CrossMark

JℲM PAPERS

Interaction between near-wall streaks and large-scale motions in turbulent channel flows

Zisong Zhou[1], Chun-Xiao Xu[1],† and Javier Jiménez[2]

[1]AML, Department of Engineering Mechanics, Tsinghua University, Beijing 100084, PR China
[2]School of Aeronautics, Universidad Politécnica de Madrid, 28040 Madrid, Spain

The interactions between the near-wall streaks and the large-scale motions (LSMs) of the outer region of wall-bounded turbulent flows are investigated. The co-supporting hypothesis of Toh & Itano (*J. Fluid Mech.*, vol. 524, 2005, pp. 249–262) is checked in full-scale channels at low to moderate Reynolds numbers, from two points of view. To study the top-down influence of the outer structures on the spanwise motion of the near-wall streaks, a method inspired by particle-image velocimetry is used to track the spanwise position of the streaks. Their spanwise advection velocity is found to be affected by the hierarchy of large-scale circulations in the logarithmic layer, but their spanwise streak density is only weakly related to the LSMs. The evidence suggests that a top-down influence exists and drives the drift of the streaks in the spanwise direction, as suggested by Toh & Itano (*J. Fluid Mech.*, vol. 524, 2005, pp. 249–262), but that the hypothesised streak accumulation rarely occurs. Numerical experiments at $Re_\tau \approx 535$ are then performed to clarify the role of the near-wall streaks in the generation and preservation of the outer LSMs. The results show that the merger of the near-wall streaks is only weakly correlated with the generation of the LSMs, and that removing the near-wall roots of the LSMs does not affect the evolution of their outer region. It is concluded that the bottom-up influence from the near-wall streaks is not essential for the LSM generation and preservation, also weakening the evidence for the co-supporting hypothesis.

Key words: turbulent boundary layers, turbulence simulation

1. Introduction

Coherent structures in wall-bounded turbulent flows play vital roles in turbulence production and maintenance. Velocity streaks and quasi-streamwise vortices are the two dominant structures in the near-wall region. Their cyclic generation consists of a self-sustaining process (Jiménez & Moin 1991; Hamilton, Kim & Waleffe 1995), which

† Email address for correspondence: xucx@mail.tsinghua.edu.cn

can survive in the absence of turbulence in the outer region (Jiménez & Pinelli 1999). In recent years, large-scale motions (LSMs), as well as very-large-scale motions (VLSMs) in the logarithmic and outer regions, have been evidenced and received extensive attention (Jiménez 1998; Kim & Adrian 1999; del Álamo & Jiménez 2003; del Álamo *et al.* 2004; Guala, Hommema & Adrian 2006; Balakumar & Adrian 2007; Hutchins & Marusic 2007*a*; Monty *et al.* 2009). They are characterised by streamwise elongated large-scale low- and high-speed regions and counter-rotating roll cells. The LSMs have a streamwise length of approximately $h \sim 3h$ (Adrian 2007), whereas the VLSMs can be as long as $O(10h)$ and as wide as $O(h)$, where h denotes the outer length scale, such as the boundary layer thickness, half-channel height or pipe radius. They not only carry more than half of the turbulent kinetic energy, but also a large fraction of the Reynolds shear stress (Guala *et al.* 2006). They are active and participate deeply in the dynamics of wall turbulence. However, the origin of the LSMs and VLSMs, and their relation to near-wall structures are far from being settled, and further investigation is needed.

A hypothesis proposed by Kim & Adrian (1999) attributes the generation of LSMs to the alignment of hairpin vortices in the near-wall region. Vortex packets that carry a low-momentum zone inside are assumed to induce much longer low-speed streaks as they propagate downstream and lift the mean shear. Near-wall structures are suggested to provide conditions for the LSM generation (Adrian 2007). This bottom-up hypothesis has been evidenced by the subsequent researches in boundary layer flows (Lee & Sung 2011) and pipe flows (Baltzer, Adrian & Wu 2013). Doohan, Willis & Hwang (2021) also proposed a possible larger-scale eruption mechanism in the near-wall region, in terms of subharmonic streak instability. This mechanism may lead to the formation of the wall-reaching part of high-speed large-scale streaks, although the result is limited to the buffer layer and the nearby scales.

Another hypothesis holds that the genesis of LSMs is the result of linear energy amplification independent of the flow in the near-wall region. Butler & Farrell (1993) and del Álamo & Jiménez (2006) revealed that the LSMs can be described well by the linear modes with the largest transient growth. Pairs of large-scale counter-rotating roll cells, similar to the widely documented statistical organisation of turbulent flow, were observed in their research, and similar findings by Pujals *et al.* (2009) and McKeon & Sharma (2010) provide further support. Based on this hypothesis, a possible self-sustaining mechanism of LSMs in the absence of near-wall structures was put forward, for example, by Flores & Jiménez (2006), who showed that the structures in the outer region remain virtually unchanged after adding wall disturbances, regardless of the near-wall condition. This agrees with the earlier conjecture by Townsend (1976) that the effect of wall roughness on the structure of turbulence does not extend beyond a thin roughness layer. Hwang & Cossu (2010) and Cossu & Hwang (2017) found that LSMs can self-sustain when the small-scale motions are artificially quenched, agreeing with older conclusions from the observation of large scales in large-eddy simulations of channel flow (Scovazzi, Jiménez & Moin 2001). Considering the similar self-sustaining process of near-wall structures, these results suggest that dynamics of the structures at each relevant scale are mostly controlled by the local mean shear through a linear amplification mechanism, rather than by the interaction with larger or smaller scales. In fact, Mizuno & Jiménez (2013), Dong *et al.* (2017) and Kwon & Jiménez (2021) have shown that LSMs very similar to those in wall turbulence exist even in the absence of a wall, and Tuerke & Jiménez (2013) showed that small artificial changes in the off-wall shear in channels have strong structural effects consistent with a local origins of the LSMs.

Beyond the different opinions on their origin, the influence of LSMs and VLSMs on the near-wall region is widely documented. The footprint of large-scale structures

reach deeply into the near-wall region (Hoyas & Jiménez 2006; Hutchins & Marusic 2007*b*), and this top-down influence was categorised into superposition and amplitude modulation by Mathis, Hutchins & Marusic (2009). Superposition is a linear process that refers to the contribution of the footprint of LSMs to turbulent kinetic energy in the near-wall region (Hoyas & Jiménez 2006; Marusic, Mathis & Hutchins 2010*a*). Amplitude modulation is a nonlinear process that describes how small-scale turbulent fluctuations are enhanced in large-scale high-speed regions and suppressed in low-speed ones. A predictive model for the streamwise velocity fluctuations in the near-wall region has been proposed based on large-scale signals from the logarithmic layer (Marusic, Mathis & Hutchins 2010*b*; Mathis, Hutchins & Marusic 2011). Turbulent statistics are well predicted by this model. Abe, Kawamura & Choi (2004) also proposed a possible top-down influence on the wall-shear stress fluctuations. The positive and negative dominant regions of the streamwise wall-shear stress fluctuations were found to be corresponding with the high- and low-speed regions of the VLSMs, respectively, whereas the active regions of the spanwise wall-shear stress tend to concentrate under high-speed regions of the VLSMs, suggesting the possible top-down influence on the spanwise velocity fluctuations.

According to the hypothesis of hairpin packets, the near-wall region provides the environment for the generation of LSMs. Combining the bottom-up hypothesis with the top-down mechanism, it is conceivable that a co-supporting mechanism exists that involves the near-wall structures and the LSMs of the outer flow. Such a hypothesis was proposed by Toh & Itano (2005), who studied the correlation between spanwise motions of near-wall streaks and outer large-scale structures in a streamwise-minimal channel. In it, the large-scale circulations carry near-wall low-speed streaks toward up-washing regions, and low-speed LSMs are generated by the merger and eruption of the near-wall streaks in the areas where they concentrate. In down-washing regions, the outer-layer circulation continually carries fluid towards the wall, enhancing the wall shear, and near-wall streaks are created due to instabilities. The co-supporting cycle is completed when these two processes are connected by the large-scale counter-rotating roll cells, and provides an intuitive framework for the inner–outer interaction, in which the distribution of near-wall streaks matches the LSMs in the spanwise direction.

However, the simulations of Toh & Itano (2005) suffer from a low Reynolds number and a short computational domain. There lacks solid mathematical description of the hypothesised co-supporting cycle, and whether the hypothesis holds is still an open question. This motivates the present study, in which conditional statistics and numerical experiments are designed to further elucidate this issue. Its main purpose is to examine and verify whether the co-supporting hypothesis survives in full-sized turbulent channel flows at higher Reynolds numbers by checking its hypothesised bottom-up and top-down branches, as well as to quantify the effect of those branches on the flow.

The paper is organised as follows. The direct numerical simulation (DNS) data used in the present study is described in § 2. The trajectories of the spanwise locations of the near-wall streaks in full-sized turbulent channels are analysed in § 3. The top-down influence of the outer flow on the motion and density of the streaks is examined and quantified in §§ 3.1 and 3.2. Numerical experiments are performed in § 4 to investigate the possible bottom-up influence of the near-wall structures on the generation and maintenance of the outer LSMs, and conclusions are offered in § 5.

2. DNS database of the turbulent channel flows

We use the DNS database of turbulent channel flow from del Álamo & Jiménez (2003) and Lozano-Durán & Jiménez (2014*a*). The flow is established between two parallel plates

Case	Re_τ	L_x	L_z	Δ_x^+	Δ_z^+	$(\Delta_y)_{max}^+$	TU_m/h	Reference
L550	547	$8\pi h$	$4\pi h$	13.4	6.8	6.7	172.4	del Álamo & Jiménez (2003)
M950	932	$2\pi h$	πh	11.5	5.7	7.7	276.8	Lozano-Durán & Jiménez (2014*a*)
M2000	2009	$2\pi h$	πh	12.3	6.2	8.9	113.9	Lozano-Durán & Jiménez (2014*a*)
M4200	4179	$2\pi h$	πh	12.8	6.4	10.7	90.9	Lozano-Durán & Jiménez (2014*a*)
W535	535	$2\pi h$	$4\pi h$	11.8	5.9	8.8	200.0	Deng & Xu (2012)

Table 1. Computational parameters, as detailed in the text. Here Δ_x and Δ_z are the resolution in the wall parallel directions, expressed in terms of Fourier modes, and Δ_y is the collocation resolution in the wall-normal direction. We use TU_m/h to denote the sampling time period used in the statistics of § 3. The sampling time periods T of the two numerical experiments in § 4 are $150h/U_m$ and $45h/U_m$, respectively.

separated by $2h$, at Reynolds number, $Re_\tau = u_\tau h/\nu$, ranging from 547 to 4179. The friction velocity u_τ and the kinematic viscosity ν define wall units, denoted by a '+' superscript. Quantities without explicit units are assumed to be normalised with the average bulk velocity, U_m, and with h. The streamwise, wall-normal and spanwise coordinates are x, y and z, respectively, and the flow is assumed to be periodic in the streamwise and spanwise directions, with periods L_x and L_z, respectively. The corresponding velocities are u, v and w. The numerical code is Fourier-spectral in these wall-parallel directions, and either uses Tchebychev polynomials or high-order compact finite differences in the wall-normal direction. The main numerical parameters are listed in table 1, and the reader is directed to the original publications for further details.

The simulation in the last line in table 1 is used as a reference in the series of numerical experiments in § 4, and is discussed in more detail in that section.

3. Spanwise location and drift of the near-wall streaks

As explained in § 1, the Toh & Itano (2005) co-supporting cycle consists of bottom-up and top-down branches. See the sketch in figure 1. The current section is concerned with the top-down process, according to which the spanwise drift of the near-wall streaks is driven by the large-scale streamwise rollers of the outer flow. Streaks are driven away from regions of downwash, migrate sideways and concentrate in regions of upwash. Our first attempt at locating and defining streaks was to use the method in Toh & Itano (2005). The spanwise location $z = \zeta(t, x_r, y)$ of a meaningful low-speed streak is determined by

$$u^{(2D)}(t, x, y, z)|_{x=x_r, z=\zeta} < U(y), \tag{3.1}$$

$$\frac{\partial u^{(2D)}}{\partial z}(t, x, y, z)|_{x=x_r, z=\zeta} = 0, \quad \frac{\partial^2 u^{(2D)}}{\partial z^2}(t, x, y, z)|_{x=x_r, z=\zeta} > 0, \tag{3.2a,b}$$

where the locally averaged instantaneous streamwise velocity,

$$u^{(2D)}(t, x_r, y, z) = \frac{1}{\Delta x} \int_{x_r-\Delta x/2}^{x_r+\Delta x/2} u(t, x, y, z) \, dx, \tag{3.3}$$

is used instead of u itself. Here x_r is the midpoint of the streamwise averaging interval and its determination will be discussed in detail in the following. A similar definition is used elsewhere for other velocity components, $v^{(2D)}$ and $w^{(2D)}$. Condition (3.1) guarantees that $u^{(2D)}$ is slower than the mean velocity $U(y)$, and (3.2a,b) ensures that ζ is a spanwise minimum of $u^{(2D)}$.
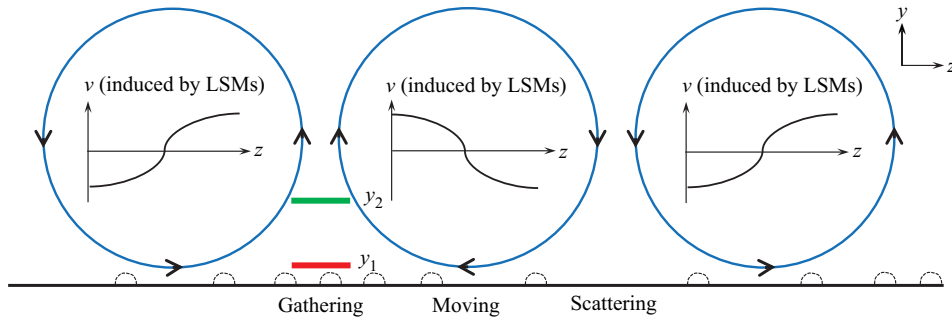
Figure 1. Sketch of the outer–inner interaction between large-scale streamwise rollers (blue circles) and the near-wall low-speed streaks (dashed curves), according to the co-supporting hypothesis in Toh & Itano (2005). The red and green lines denote the two wall-parallel observation windows, $y = y_1$ and y_2, respectively, used in §§ 3.1 and 3.2.

The choice of the averaging interval $(x_r − \Delta x/2, x_r + \Delta x/2)$ is important. Toh & Itano (2005), who analysed a streamwise-minimal channel with $L_x^+ = 384$, used the full streamwise period $\Delta x = L_x$ as their averaging length. This length is shorter than most streaks, which were thus treated as being infinitely long. Their evolution takes place in time rather than in space, and the same group later showed that the length of the near-wall streaks in a full channel can be substituted by their lifetime in a streamwise-minimal one (Abe, Antonia & Toh 2018).

We analyse in this section full-sized channels at substantially higher Reynolds numbers than in either of the two papers above, and some modifications are needed to (3.1)–(3.3). The typical streamwise length of the near-wall streaks, ℓ_{xu}, is a few thousand wall units (Hoyas & Jiménez 2006), and averaging over longer segments risks mixing streaks and hiding their spanwise meandering. We use in this paper $\Delta x^+ \approx 380$–450, which is short enough to retain structural information, but long enough to differentiate the near-wall streaks from velocity fluctuations of smaller scale. A posteriori tests show that the results below are robust in the range $\Delta x^+ \approx 300$–500.

When $\Delta x = L_x$, the streamwise origin, x_r, of the observation box becomes irrelevant, and the near-wall streaks in the streamwise-minimal flow in Toh & Itano (2005) form branching structures that tend to merge beneath large-scale low-speed regions, supporting their assumed relation between LSMs and the spanwise drift of the streaks. In larger channels, the position of the observation window is crucial. Kim & Hussain (1993) and del Álamo & Jiménez (2009) showed that the streamwise advection velocity of most quantities in the buffer layer is $u_{ad}^+ \approx 10$, and Lozano-Durán & Jiménez (2014b) later showed that $u_{ad}^+ \approx 8$ for the ejections associated with the low-speed streaks. Farther from the wall, the small scales move approximately with the mean flow velocity, with ejections also moving slightly more slowly than the flow (Lozano-Durán & Jiménez 2014b). For example, ejections at $y^+ = 200$ move at $u_{ad}^+ = 16.7$ while $U(y)^+ = 18.2$. Centring on the buffer layer, we show that the spanwise drift velocity of the streaks is of the order of u_τ, so that, if the observation window were fixed to the wall, streaks would only be observed over times of the order of $\Delta t^+ \approx \ell_{xu}^+/8 \approx 100$, during which they would drift at most by $\delta z^+ \approx 100$. This is too little to characterise the interactions in which we are interested, which involve VLSMs whose width is $\Delta z \approx h$. Therefore, we track individual streaks by moving the window with their average advection velocity, $x_r = x_{r0} + u_{ad}t$, where x_{r0} is the initial window position.
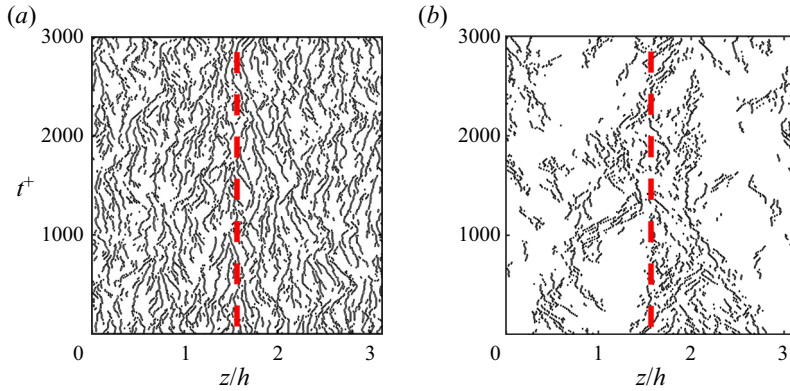
Figure 2. Time history of the spanwise locations of low-speed streaks in a full-sized channel (M950). Locations of the low-speed streaks are determined by the condition (3.1)–(3.3): (*a*) $y^+ = 5$ and (*b*) $y^+ = 200$. The red dashed line denotes the averaged location of a large-scale streak.

A typical time history of the spanwise location of low-speed streaks at $y^+ = 5$ is displayed in figure 2(*a*), using $u_{ad}^+ = 8$ as representative of the near-wall region. Each line in the figure represents the trajectory of a single low-speed streak, and it is clear from the figure that they substantially drift spanwise. Their mean spanwise spacing, approximately 100 wall units, agrees well with the known streak spacing near the wall (Smith & Metzler 1983). Toh & Itano (2005) classify the trajectories that they observe in streamwise-minimal channels into dominant branches with long lifetimes (of the order of 1000–3000 wall units), and subordinate ones with shorter lifetimes that tend to merge into the dominant ones. The lifetime of such a fragile object as a near-wall streak is hard to define, but Lagrangian scales of 300–1000 temporal wall units were obtained in the buffer layer by Jiménez *et al.* (2005), Flores & Jiménez (2010) and Abe *et al.* (2018). The lifetime of the branches in figure 2(*a*) is of the same order, 200–800 wall units, and few of them last beyond 1000 viscous time units. They thus correspond to the subordinate branches in Toh & Itano (2005).

Figure 2(*b*) is drawn at $y^+ = 200$, using $u_{ad}^+ = 16.7$, and represents the logarithmic region. The trajectories cluster in a wide band around $z/h = 1.7$, marked by a red dashed line, which appears to be one of perhaps two large streaks that dominate the flow at that level. The interpretation of this figure needs some comment. Although it is known that outer-layer low-speed regions in channels contain more small-scale vortices than high-speed ones (Tanahashi *et al.* 2004), which could be interpreted as supporting the gathering action hypothesised by Toh & Itano (2005), the clustering in figure 2(*b*) is probably an artefact of the detection criterion (3.1). Low-velocity streaks are only recognised as such when they ride on a deeper large streak that lowers their velocity below the mean profile, and what we see in the figure is probably the root of an attached streak centred farther from the wall.

The influence of criterion (3.1) should thus be further discussed. Figure 3 repeats figure 2 without using (3.1). At $y^+ = 5$, condition (3.1) discards part of the scattered dots, which reappear in figure 3, but there are also more coherent streaks in the new figure than in the old one. The spanwise drift of the streaks is present in both figures, but it is evident from comparing them that the streak density measured by (3.1)–(3.2*a*,*b*) may be influenced by (3.1). For the result at $y^+ = 200$ in figures 2(*b*) and 3(*b*), the condition (3.1) takes a dominant role, and rejects approximately half the local minima. When it is
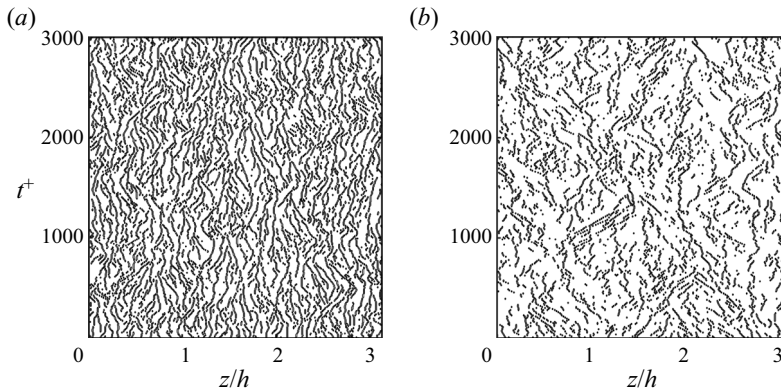
940 A23-6

(*a*) (*b*)

Figure 3. Time history of the spanwise locations of low-speed streaks in a full-sized channel (M950) without the criterion (3.1): (*a*) $y^+ = 5$ and (*b*) $y^+ = 200$.

removed, the gathering action suggested by the co-supporting is still observed, although less clearly than before, but it is not reflected in the streak density. Figure 3 shows an almost uniform distribution of small streaks, instead of only the part riding on the larger outer streak. Only condition (3.2*a,b*) will be used to define the near-wall streaks in the quantitative analysis in the next two sections.

3.1. *Spanwise drift of the near-wall streaks versus the outer eddies*

Although figures 2 and 3 clearly indicate that the streaks move spanwise, relating their drift to the outer large-scale circulations requires quantitative analysis. The premise of the top-down branch of the co-supporting cycle in Toh & Itano (2005) is that the near-wall streaks are scattered away from the down-washing regions of the large-scale circulations, and gather in the up-washing ones, as sketched in figure 1. This implies a positive correlation between the spanwise derivative, $\partial v / \partial z$, of the wall-normal velocity of the outer flow and the spanwise drift of the near-wall streaks. A positive spanwise streak velocity near the wall would correspond to a counter-clockwise large-scale circulation, in which $\partial v / \partial z > 0$ near the z-positions of the roller centres, as depicted by the first and third rolls in figure 1. A negative streak drift velocity would be associated with $\partial v / \partial z < 0$.

To quantify how streaks move as a function of their location, (t, x_r, y_1, z_s), we track the evolution of patterns of $u^{(2D)}$, using a method similar to particle-image velocimetry (PIV). Consider a one-dimensional interrogation window, $z_s - \Delta \zeta / 2 < z < z_s + \Delta \zeta / 2$, which is advected streamwise with the velocity discussed in the previous section. The streak displacement after Δt is defined as the position, δz_{max}, of the maximum of the correlation

$$R_{u^{(2D)}}(\delta z, \Delta t) = \frac{1}{(I_0 I_1)^{1/2}} \int_{z_s - \Delta \zeta / 2}^{z_s + \Delta \zeta / 2} u^{(2D)}(t, x_r, y_1, z) u^{(2D)}(t + \Delta t, x_r$$
$$+ u_{ad} \Delta t, y_1, z + \delta z) \, dz, \qquad (3.4)$$

where I_0 and I_1 are, respectively, the mean squares of $u^{(2D)}(t, x_r, y_1, z)$ and $u^{(2D)}(t + \Delta t, x_r + u_{ad} \Delta t, y_1, z + \delta z)$, averaged over the same window as in (3.4). In addition, we only accept maxima for which $R_{u^{(2D)}}(\delta z_{max}) > 0.8$. The spanwise advection velocity is defined as $w_s = \delta z_{max} / \Delta t$, and is assigned to the window centre (x_r, z_s). The following discussion focuses on the near-wall streaks at $y_1^+ = 13$. It uses $\Delta \zeta^+ \approx 50$, and an
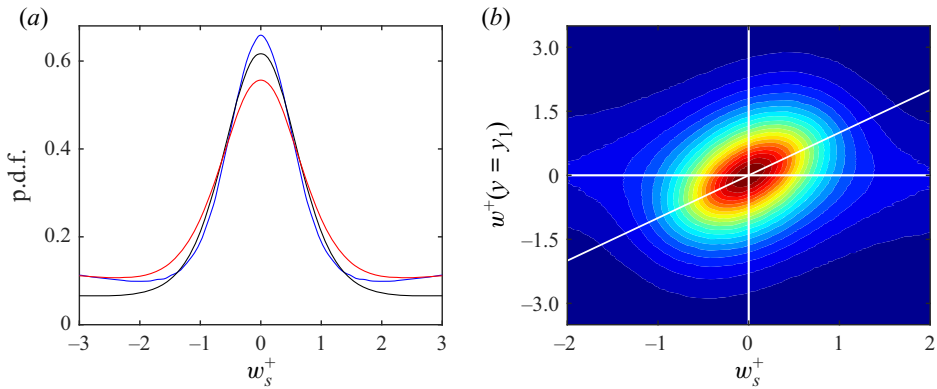
940 A23-7

Z. Zhou, C.-X. Xu and J. Jiménez

Figure 4. (a) Probability density function (p.d.f.) of w_s^+ at different Re_τ with $\Delta t^+ \approx 20$, and $u_{ad}^+ = 8$: blue solid line, Case W535; black solid line, M950; red solid line, M2000. (b) Joint p.d.f. of the streak spanwise advection velocity, w_s^+, and the spanwise velocity fluctuations, w^+ at $y_1^+ = 13$. Case M950, and $\Delta t^+ = 20$. The white diagonal is $w^+ = w_s^+$.
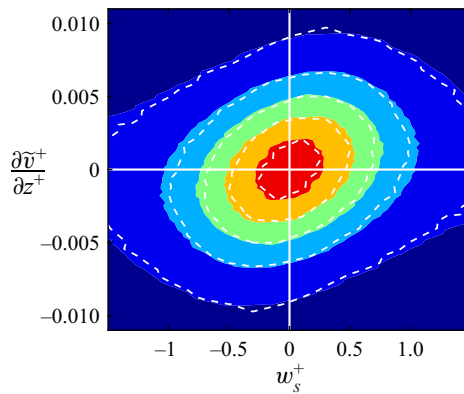

Figure 5. Joint p.d.f. of the spanwise drift velocity w_s^+ at $y_1^+ = 13$ and $\partial \tilde{v}^+/\partial z^+$ at $y_2^+ = 200$: shaded, w_s^+ by PIV; white dashed lines, w_s^+ at the streak centres. Contour levels are 0.1(0.2)0.9 of the maximum probability density. Case M950, $\Delta t^+ \approx 20$ and $\Delta z^+ = 214$.

advection velocity of the interrogation window $u_{ad}^+ = 8$, as in figure 2(a). The results are robust in the range $\Delta \zeta^+ \in [30, 70]$, and the effect of Δt^+ and u_{ad}^+ is discussed in Appendix A.

The probability density function (p.d.f.) of the drift velocity at different Re_τ shown in figure 4(a) is concentrated approximately in the range $w_s^+ = [-2, 2]$, independently of the Reynolds number. This is the same order of magnitude as the spanwise velocity fluctuations of the flow, and the two quantities are closely related. The joint p.d.f. of w_s^+ and w^+ at $y_1^+ = 13$ is displayed in figure 4(b) for case M950. It shows a clear correlation between the two variables, providing direct evidence that the drift of the streaks is not due to their internal dynamics, but to the ambient flow.

We next turn our attention to the correlation of the drift velocity with the structures of the outer flow, represented by the wall-normal velocity at $y_2 > y_1$, smoothed with a top-hat

940 A23-8

filter to isolate the large-scale component,

$$\tilde{v}(x_0, y_2, z_0) = \frac{1}{\Delta z} \int\limits_{z_0-\Delta z/2}^{z_0+\Delta z/2} v^{(2D)}(x_0, y_2, z) \, \mathrm{d}z, \tag{3.5}$$

where $v^{(2D)}$ is defined as in (3.3). A typical joint p.d.f. is shown in figure 5. The abscissae are w_s at $y_1^+ = 13$, and the ordinates are the spanwise derivative of $\tilde{v}$ at $y_2^+ = 200$. It is evident that the p.d.f. is preferentially aligned to the first and third quadrants, i.e. that a positive spanwise drift of the streaks tends to occur beneath positive $\partial \tilde{v}/\partial z$, and vice versa, in agreement with the top-down model. To verify that the continuous velocity field obtained by the PIV method truly represent the drift of the streaks, the joint p.d.f., using w_s^+ collected at the points identified by (3.2a,b) as the streak centres, are also shown by the white contours in figure 5 for comparison. The differences with the PIV results are negligible.

The mutual dependence of the two quantities can be quantified by the correlation coefficient

$$R\left(w_s, \frac{\partial \tilde{v}}{\partial z}\right) = \frac{\sum w_s \dfrac{\partial \tilde{v}}{\partial z}}{\left[\sum w_s^2 \sum \left(\dfrac{\partial \tilde{v}}{\partial z}\right)^2\right]^{1/2}}. \tag{3.6}$$

Appendix A shows that $R(w_s, \partial \tilde{v}/\partial z)$ depends on the PIV parameters, and on the wall-normal positions y_2 of the outer-flow. For the case in figure 5, the correlation of the two quantities is $R_{w_s, \partial \tilde{v}/\partial z} \approx 0.2$, but it can be raised to the order of 0.4 as y_2 changes. See Appendix A for the details.

In fact, one of the functions of the window used to define w_s and $\tilde{v}$ is to highlight how the correlation depends on the spanwise wavelength and on the distance from the wall. The top-down correlations considered by Toh & Itano (2005) and Abe *et al.* (2018) were restricted to outer scales with $\lambda_z \sim h$, but it makes sense to also consider interactions with intermediate scales presenting in the logarithmic layer, for which $100 \lesssim \lambda_z^+$ and $\lambda_z \lesssim h$. Consider the inertia tensor of the joint p.d.f. of w_s and the unfiltered $\partial v/\partial z$, defined as

$$I\left(w_s, \frac{\partial v}{\partial z}\right) = \begin{pmatrix} I_{w_s w_s} & I_{w_s(\partial v/\partial z)} \\ I_{(\partial v/\partial z)w_s} & I_{(\partial v/\partial z)(\partial v/\partial z)} \end{pmatrix}, \tag{3.7}$$

where

$$I_{ab} = \frac{1}{L_x L_z} \iint a(x, z) b(x, z) \, \mathrm{d}z \, \mathrm{d}x. \tag{3.8}$$

To isolate the spanwise scale, express each variable as its Fourier transform along z, using $\hat{\varphi}(t, x, y, k_z)$ to represent the Fourier coefficient of $\varphi(t, x, y, z)$ at the spanwise

wavenumber k_z. The different moments can be expressed as integrals over k_z,

$$I_{w_s w_s} = \int \widehat{w}_s \widehat{w}_s{}^* \, \mathrm{d}k_z, \tag{3.9}$$

$$I_{(\partial v/\partial z)(\partial v/\partial z)} = \int \mathrm{i}k_z \hat{v}(\mathrm{i}k_z \hat{v})^* \, \mathrm{d}k_z = \int k_z^2 (\hat{v}\hat{v}^*) \, \mathrm{d}k_z, \tag{3.10}$$

$$I_{w_s(\partial v/\partial z)} = I_{(\partial v/\partial z)w_s} = \int \mathrm{Re}(\mathrm{i}k_z \hat{v}\widehat{w}_s{}^*) \, \mathrm{d}k_z = \int \mathrm{Re}(\widehat{w}_s(\mathrm{i}k_z \hat{v})^*) \, \mathrm{d}k_z$$

$$= \int -k_z \mathrm{Im}(\hat{v}\widehat{w}_s{}^*) \, \mathrm{d}k_z, \tag{3.11}$$

where the '$*$' superscript denotes complex conjugation, and averaging over x is implied everywhere. A spectral inertia tensor can then be defined for each k_z as

$$I\left(w_s, \frac{\partial v}{\partial z}; k_z\right) = \begin{pmatrix} \widehat{w}_s \widehat{w}_s{}^* & -k_z \mathrm{Im}(\hat{v}\widehat{w}_s{}^*) \\ -k_z \mathrm{Im}(\hat{v}\widehat{w}_s{}^*) & k_z^2(\hat{v}\hat{v}^*) \end{pmatrix}. \tag{3.12}$$

We are interested in the relation of k_z with the height at which $\hat{v}(k_z)$ has the strongest influence on w_s. The strength of this influence can be quantified by the inclination angle θ of the principal axes of the joint p.d.f. inertia ellipse, and $\theta = \arctan|a_2/a_1|$ can be calculated from the leading eigenvector (a_1, a_2) of the inertia tensor. Here we can define a rescaled tensor that avoids derivatives by removing the k_z factors from I, for k_z in (3.12) not only bring dimensional complications, but also has a scale-dependent influence on the principal axes:

$$I(w_s, v; k_z) = \begin{pmatrix} \widehat{w}_s \widehat{w}_s{}^* & -\mathrm{Im}(\hat{v}\widehat{w}_s{}^*) \\ -\mathrm{Im}(\hat{v}\widehat{w}_s{}^*) & \hat{v}\hat{v}^* \end{pmatrix}. \tag{3.13}$$

This tensor directly relates the velocities at the two wall distances at scale k_z, and has the advantage of balancing their magnitudes and dimensions. Note that the imaginary part in the off-diagonal elements of (3.13) has the effect of translating spanwise one of the variables by a quarter wavelength with respect to the other, so that $I(w_s, v; k_z)$ describes the correlation of the streak drift velocity with the shifted wall-normal velocity in the outer flow.

The inclination angle θ determined by the second and first components of the leading eigenvector of (3.13), with $0 < \theta < \pi/2$, quantifies the magnitude of the v fluctuations at y_2, relative to the drift velocity of the near-wall streaks with which they correlate. The location, y_2 of the maximum for each wavelength, $\lambda_z = 2\pi/k_z$, can be taken to represent the distance from the wall of the centre of the rollers with that spanwise dimension. It is displayed in figure 6, which clearly shows that rollers are most effective at advecting streaks over distances similar to their own height (of the order of $\lambda_z \approx 4y_2$). For example, the maximum correlation in figure 17 in Appendix A is obtained when the wall-normal velocity is smoothed with a filter for which $\Delta z^+ \approx 200$ at $y_2^+ = 100$. As the effect of the eddies responsible for this correlation reaches, by definition, the near-wall region, the self-similar dependence of their size is one more demonstration of the attached-eddy model of Townsend (1961), and proves that the buffer-layer streaks are not controlled by eddies of a single size, but by the whole hierarchy of attached structures of the logarithmic layer.
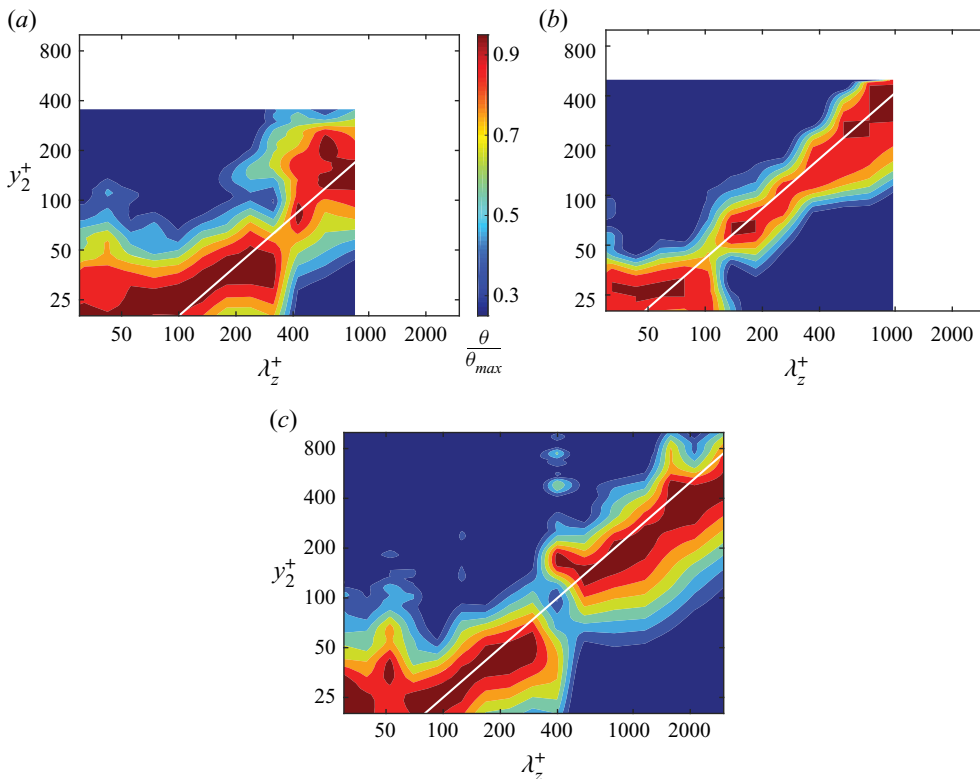
(*a*)

(*b*)

(*c*)

Figure 6. Inclination angle, θ/θ_{max}, of the leading eigenvector of the correlation tensor (3.13), as function of y_2 and of the spanwise wavelength λ_z, where θ_{max} is the maximum of θ at the corresponding wavelength: (*a*) W535; (*b*) M950; (*c*) M2000.

3.2. *Near-wall streak density and the outer region*

Having established the influence of the outer structures on the spanwise drift of the streaks of the buffer layer, it remains to be shown whether this drift results in the modulation of the density of streaks. This assumption underlies the second, bottom-up, branch of the co-supporting hypothesis of Toh & Itano (2005), which proposes that the accumulation of low-speed streaks below an existing outer-flow ejection leads to some kind of collective instability that reinforces the ejection. At first sight, this conclusion is reasonable, because the streaks converge where $\tilde{v}(y_2) > 0$ and diverge where $\tilde{v}(y_2) < 0$. However, the density of streaks not only depends on their motion, but also on the rate at which they are born and disappear, and it should be clear from the discussion in § 3 that the longest reasonable lifetime of a streak is of the same order as the time required for it to drift across distances of order h. In fact, a cursory inspection of figure 3 shows that most streaks do not live long enough to cross spanwise distances of the order of the width of the largest VLSMs, but, because we saw at the end of § 3.1 that streaks also interact with narrower structures closer to the wall, we need to determine whether the same conclusion applies to these structures. In this section we examine directly the correlation of the outer $\tilde{v}$ with the density of buffer-layer streaks.

To quantify this correlation, we again define two spanwise windows, one at $y_1^+ = 13$ in the buffer layer, and another at y_2 in the outer region. Both windows have the same width, Δz, and are centred at the same wall-parallel location (x_0, z_0), but they serve

	L550	M950	M2000	M4200
n_x	30	15	30	61
n_z	1470	710	1470	3010
n_t	110	575	430	40
N	4.85×10^6	6.12×10^6	1.90×10^7	7.22×10^6

Table 2. Number of samples used for the streak statistics: n_x, n_z and n_t denote sample numbers in the x, z and t directions, and $N = n_x n_z n_t$ is the total number of samples.

different purposes. The inner window is used to compute the streak density by counting minima of $u^{(2D)}$, as in (3.2a,b). The outer window is used to compute the smoothed $\tilde{v}$, as in (3.5). The streamwise interval used to compute $u^{(2D)}$ and $v^{(2D)}$ is the same as in § 3, $\Delta x^+ = 400$, but several Δz are used to test their effect on the results. A minimum value for Δz can be estimated from physical arguments. As the spacing of the buffer-layer streaks is known to be approximately 100 wall units (Kline *et al.* 1967; Smith & Metzler 1983), and the hypothesis in Toh & Itano (2005) is that at least two streaks need to merge to generate a larger-scale 'eruption', it is reasonable to choose $\Delta z^+ \gtrsim 200$. Statistics are compiled by scanning x_0, z_0 and time. The number of samples in each direction is summarised in table 2. The total number of samples used for each Reynolds number always exceeds 4×10^6.

The spanwise density of streaks ρ_s is the inverse of their average spacing, and is simply determined from the number, n_s, of minima in the observation window, $\rho_s = n_s / \Delta z$. It follows from the classical estimates of streak spacing that we can expect $\rho_s^+ \approx 0.01$.

Distributions of the streak spacing are given in figure 7, compared with the results of Smith & Metzler (1983) in a turbulent boundary layer at $Re_\tau \approx 724$. Figure 7(a) shows the effect on the spacing of the size of the detection window. As expected, the distribution becomes more concentrated for wider windows, but the mode of the distribution, $\ell_{zu}^+ \approx 70$, remains constant and is only slightly narrower than the result of Smith & Metzler (1983), $\ell_{zu}^+ \approx 85$. Considering that these authors detect streaks from the accumulation of hydrogen bubbles at $y^+ = 5$, and determine visually the distance among neighbouring streaks, the discrepancy can probably be attributed to the different definitions of what constitutes a streak. Even so, the p.d.f. obtained with our narrowest window, $\Delta z^+ \approx 200$, is fairly close to that in Smith & Metzler (1983), and this window is used in the following. Figure 7(b) shows that the density distribution is essentially independent of the Reynolds number, also in agreement with Smith & Metzler (1983).

The correlation coefficient between ρ_s and $\tilde{v}$ is defined as

$$R(\rho_s, \tilde{v}) = \frac{\sum (\rho_s - \overline{\rho_s}) \tilde{v}}{\left[\sum (\rho_s - \overline{\rho_s})^2 \sum \tilde{v}^2 \right]^{1/2}}, \tag{3.14}$$

where $\overline{\rho_s^+} \approx 0.01$ denotes the averaged streak density. The averaged wall-normal velocity vanishes from continuity, and the summation extends over all the samples in table 2. The streak density ρ_s is a local quantity depending on the spanwise locations, whereas the correlations between the local ρ_s and $\tilde{v}$ could capture the possible streak accumulation. If the streaks really accumulated in the up-washing regions of $\tilde{v}$ and drained away from the down-washing regions, the correlation $R(\rho_s, \tilde{v})$ would be strongly positive. However, figure 8(a,b) show that the correlation is always smaller than 0.2, and even turns negative at large y_2, contradicting the assumption of the top-down model of Toh & Itano (2005). This failure can be traced to our rejection of condition (3.1), which was used by Toh &
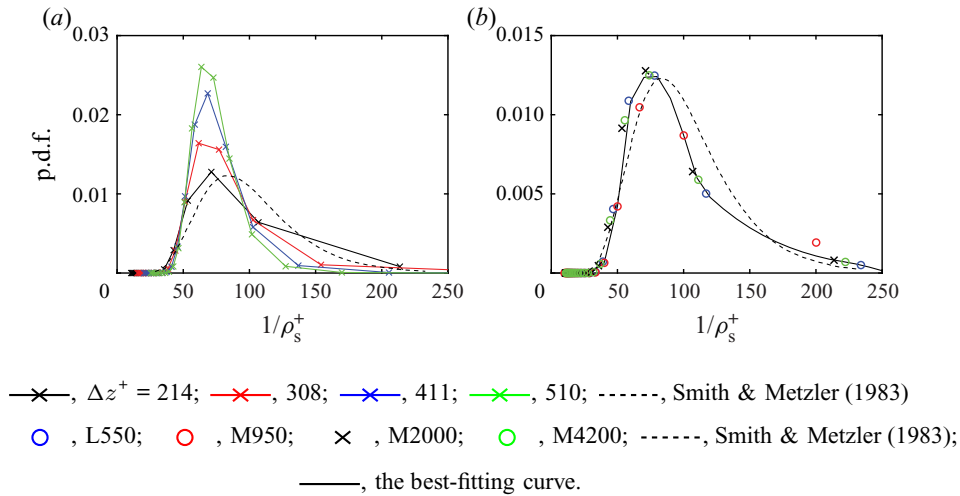
Figure 7. (*a*) Probability density function of the streak density at different Δz in case M2000: black, $\Delta z^+ = 214$; red, $\Delta z^+ = 308$; blue, $\Delta z^+ = 411$; green, $\Delta z^+ = 510$; dashed, Smith & Metzler (1983). (*b*) Probability density function of the streak density distributions at different Re_τ and $\Delta z^+ \approx 200$: blue circles, L550; red circles, M950; black crosses, M2000; green circles, M4200; dashed line, Smith & Metzler (1983); full line, the best-fitting curve.

Itano (2005) when identifying streaks. This criterion has very little influence on the drift statistics in § 3.1, but figure 8(*c*), as well as figure 3, shows that it strongly affects the results for the streak density. The density is clearly correlated with the outer large-scale circulations when using (3.1), because that condition tends to reject streaks underneath large-scale high-speed regions, and to retain the roots of the low-speed ones. However, when only the local minimum condition (3.2*a,b*) is used, the accumulation becomes weaker or negative.

Another effect that may influence the correlation $R(\rho_s, \tilde{v})$ is the modulation of the local wall shear by the outer LSMs. A negative $\tilde{v}$ brings high-speed fluid from the outer flow towards the wall, increasing the local shear and, in effect, decreasing the local viscous length. If the streak generation process is in equilibrium with this shear, the local streak spacing should decrease and the streak density should increase. This would tend to counteract the hypothesised local decrease in density due to divergence, and decrease the inner–outer correlation. If the modulation is strong enough, it may overcome the correlation completely, and even become negative. The effect is similar to the LSM-induced local wall-shear fluctuations in Abe *et al.* (2004) and the large-scale modulations in Mathis *et al.* (2009), which were also shown in Jiménez (2012) and Zhang & Chernyshenko (2016) to be mostly reducible to scaling by the local friction velocity, $(u_\tau)_{local} = (\nu \, \partial \tilde{u}/\partial y)^{1/2}$.

Figure 9 shows that the effect is not trivial, and confirms that it is a consequence of the interaction with the outer flow. Figure 9(*a*) presents the p.d.f. of $(u_\tau)_{local}$ for three Reynolds numbers, computed over a spanwise averaging window whose size scales in wall units. The variation is of the order of $\pm 20\,\%$, and widens as the Reynolds number increases, in agreement with the increase in energy from the wider range of scales of the velocity fluctuations. If the effect were local to the near-wall layer, it would be difficult to explain this Reynolds number dependence. In fact, figure 9(*b*) shows that, when the averaging window is scaled in outer units, the variation of $(u_\tau)_{local}$ depends on the size of the window, but not on the Reynolds number.
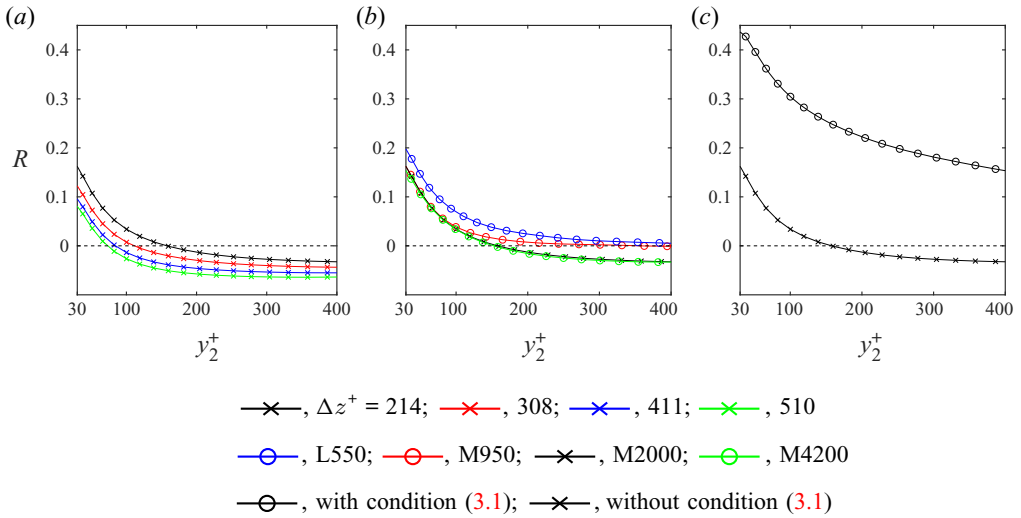
Figure 8. (*a*) Correlation $R(\rho_s, \tilde{v})$ at different Δz in case M2000: black, $\Delta z^+ = 214$; red, $\Delta z^+ = 308$; blue, $\Delta z^+ = 411$; green, $\Delta z^+ = 510$. (*b*) As in (*a*) for different Re_τ and $\Delta z^+ \approx 200$: blue, L550; red, M950; black, M2000; green, M4200. (*c*) Correlation for $\Delta z^+ = 214$ in case M2000: circles, with condition (3.1); crosses, without condition (3.1).
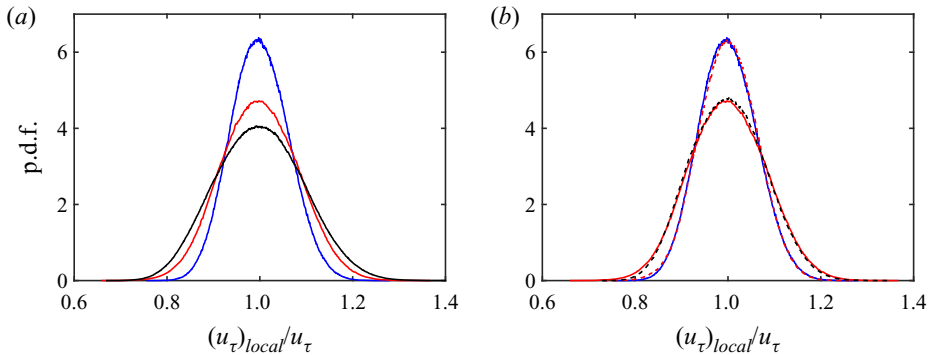

Figure 9. Probability density function of $(u_\tau)_{local}/u_\tau$ at different Re_τ, where $(u_\tau)_{local}$ is the local friction velocity computed over each window, and u_τ is its global average: (*a*) $\Delta z^+ \approx 200$; blue solid line, L550; red solid line, M950; black solid line, M2000; (*b*) $\Delta z/h \approx 0.4$; blue solid line, L550; red dashed line, M950; $\Delta z/h \approx 0.2$, red solid line, M950; black dashed line, M2000.

Finally, figure 10 shows that, when both ρ_s^+ and $\tilde{v}^+$ are scaled in the local wall units, the effect of the averaging window on $R(\rho_s^+, \tilde{v}^+)$ largely disappears, but the correlation still decays with y_2. It becomes negligible above $y_2^+ \approx 150$ but, in contrast to figures 8(*a*) and 8(*b*), it does not become negative at higher y_2. It is interesting that the limit for this decay scales in wall units, suggesting that the reason has more to do with the dynamics of the buffer layer than with the outer flow.

What needs to be explained is why streaks drift spanwise but do not accumulate, and the simplest explanation is their short lifetime, which is $t^+ = O(500)$ instead of the $t^+ = 1000$–3000 in Toh & Itano (2005). As $w_s^+ = O(1)$, their maximum drift is thus only $\delta z^+ = 300$–500 (see figure 3*a*), and the outer structures can only couple with the streak density over widths of this order. It follows from figure 6 that this corresponds to $y_2^+ \approx 100$, and
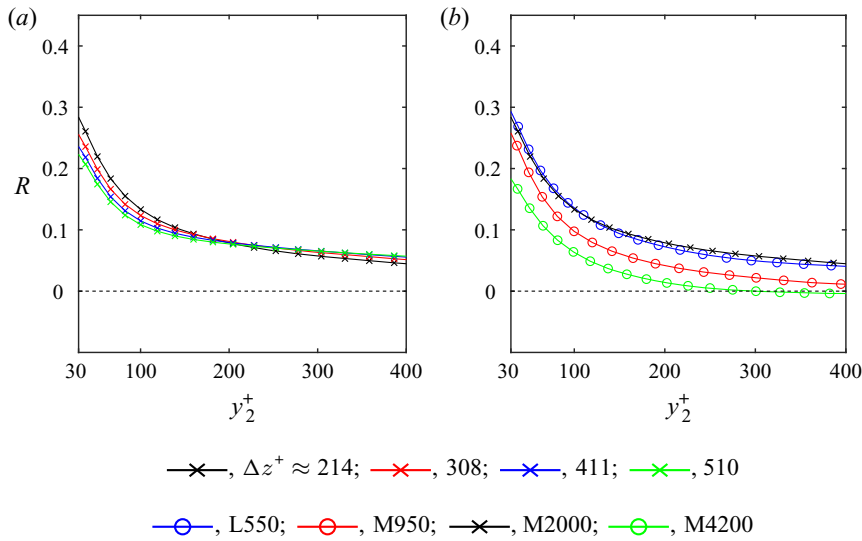
940 A23-14

Figure 10. Correlation $R(\rho_s^+, \tilde{v}^+)$ scaled in local wall units. (*a*) At different window size in case M2000: black, $\Delta z^+ \approx 214$; red, $\Delta z^+ \approx 308$; blue, $\Delta z^+ \approx 411$; green, $\Delta z^+ \approx 510$. (*b*) At different Re_τ when $\Delta z^+ \approx 200$: blue, L550; red, M950; black, M2000; green, M4200.

that the accumulation hypothesised in Toh & Itano (2005) is a wall-layer effect that should become increasingly less relevant as the Reynolds number increases.

4. Bottom-up influence on the LSM generation and preservation

In order to examine the possibility of bottom-up influence during the LSM generation process, two further numerical experiments are performed. In the first, the flow in the channel is initialised with a laminar velocity profile near the upper wall and a turbulent velocity profile near the lower wall, as in Schoppa & Hussain (2002). The initial perturbations, added below $y^+ = 50$ in the lower half of the channel, are constructed by filtering the flow in case W535 to retain the velocity fluctuations with $\lambda_z^+ < 230$. As experience shows that early flow adjustments kill part of these perturbations, they are amplified by a moderate factor (approximately 1.3) before being added to the flow, so that the near-wall Reynolds stress is similar to the fully developed one after the initial decay. This ensures that the channel transitions to turbulence, and is robust to amplification factors up to two. Part of the adjustment is the imposition of continuity by the first simulation step, which is not initially satisfied near the upper boundary of the added streaks ($y^+ = 50$), but the effect is minor. The code and computational parameters are as in W535 (see table 1), with the Reynolds number fixed to $Re = U_m h/\nu = 9800$, which corresponds to $Re_\tau \approx 535$ near the lower wall.

Before detailed quantitative analysis, it is helpful to have an overview of the development of the flow. Figure 11 shows the time history of the local Re_τ on the upper and lower walls. The lower-wall Re_τ initially decreases a bit, and then increases until $t = 20$, gradually approaching its target value of $Re_\tau = 535$. On the upper wall, the flow remains laminar until turbulent transition occurs around $t = 60$. The upper Re_τ then quickly increases until $t = 75$, after which it approaches its turbulent level, $Re_\tau = 535$. The time evolution of the mean velocity profile is displayed in figure 12, non-dimensionalised by the local wall units at the corresponding time instants. In the lower side, shown in figure 12(*a*), the
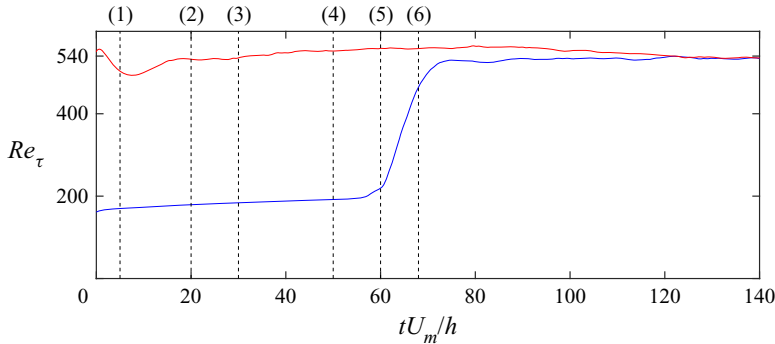
Figure 11. Time history of the local Re_τ on the upper (blue solid line) and lower (red solid line) walls. The dashed vertical lines (1)–(6) mark the corresponding time instants in figures 13 and 18: (1) $t = 5$, (2) $t = 20$, (3) $t = 30$, (4) $t = 50$, (5) $t = 60$ and (6) $t = 68$.
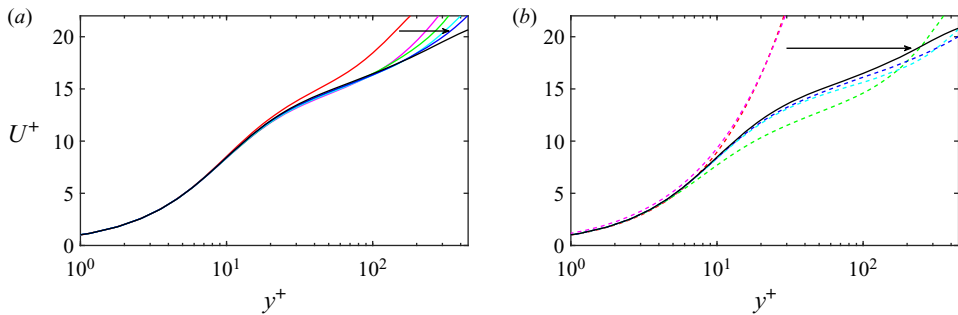

Figure 12. Time evolution of the mean velocity profile, U^+, scaled in local wall units. (*a*) In the lower half-channel from $t = 10$ to $t = 50$: red solid line, $t = 10$; pink solid line, $t = 20$; green solid line, $t = 30$; sky blue solid line, $t = 40$; blue solid line, $t = 50$. And (*b*) in the upper half-channel, from $t = 50$ to $t = 90$: red dashed line, $t = 50$; pink dashed line, $t = 60$; green dashed line, $t = 70$; sky blue dashed line, $t = 80$; blue dashed line, $t = 90$. The black lines (black solid line) denote the profile in case W535. The arrows indicate increasing time.

profile overlaps the fully developed one below $y^+ = 20$ for $t = 10$–50, and the agreement gradually extends to higher positions as time develops. This suggests that turbulent structures are gradually being constructed at higher positions as the flow approaches equilibrium. After $t = 50$, the mean velocity profile collapses to the fully developed flow. In the upper half-channel, shown in figure 12(*b*), the profile quickly changes from laminar to turbulent as that wall transitions at $t = 60$–70, as also indicated by the abrupt increase of Re_τ in figure 11. The flow continues to adjusts after $t = 80$, and the whole channel then evolves to a fully developed turbulent state.

We consider in this section the evolution of the flow structures near the lower wall, where the initial perturbations are added. The evolution of the upper half-channel is closer to classical bypass transition, and is discussed in Appendix B. The distribution of the streamwise velocity fluctuations in the lower half-channel is displayed in figure 13 at the three selected times indicated by the lines (1)–(3) in figure 11. At $t = 5$, the perturbations are confined to the near-wall region, which is dominated by small-scale velocity streaks. Turbulent fluctuations gradually spread farther from the wall, in accordance with the evolution of the velocity profile in figure 12, and streaks of increasingly larger scales
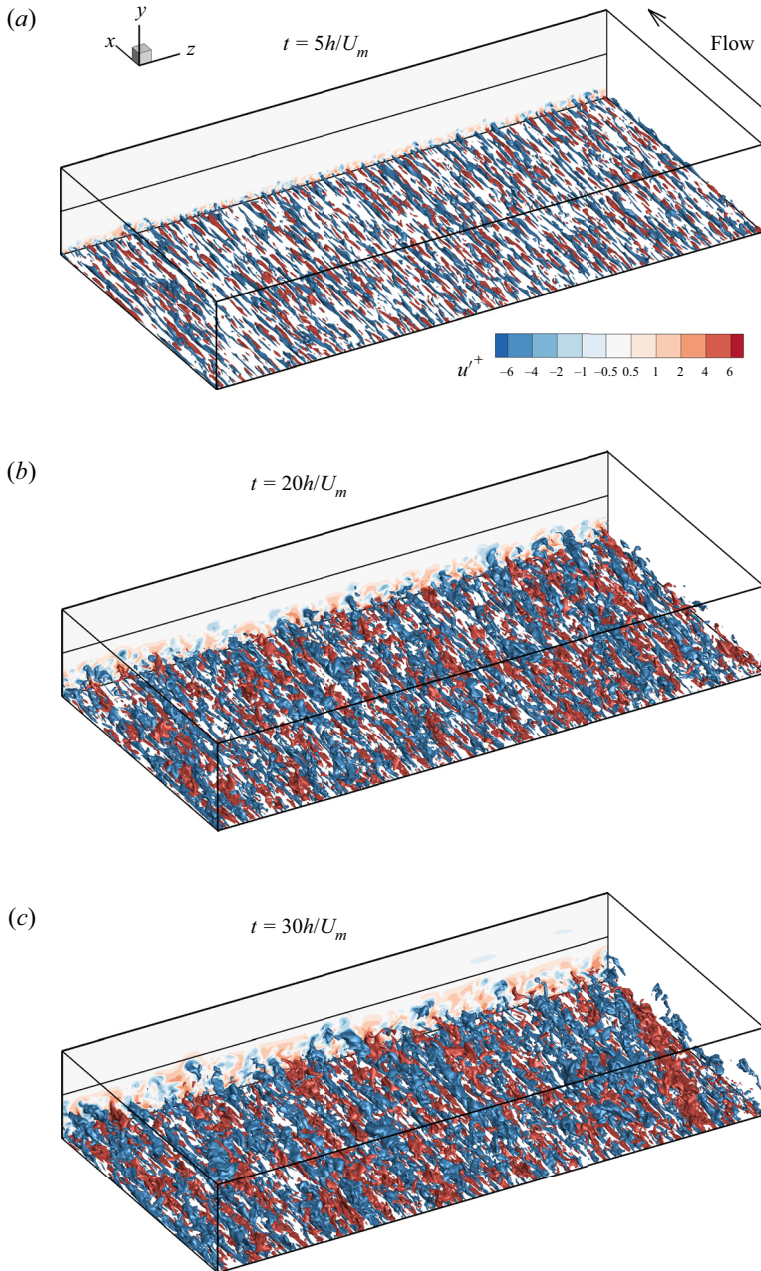
940 A23-16

Figure 13. Distributions of u' in the lower half-channel at (*a*) $t = 5$, (*b*) $t = 20$ and (*c*) $t = 30$. Length in the x direction is 2π and in the z direction is 4π. Red: $u'^+ = 3$; blue: $u'^+ = -3$. Flow is from bottom right to top left.

appear at $t = 20$ and 30. The approximate size of the largest streaks at $t = 20$ is $\lambda_z \sim 0.7h$, and they grow to $\lambda_z \sim h$ at $t = 30$. The turbulent fluctuations visually occupy the whole lower half-channel after that time.
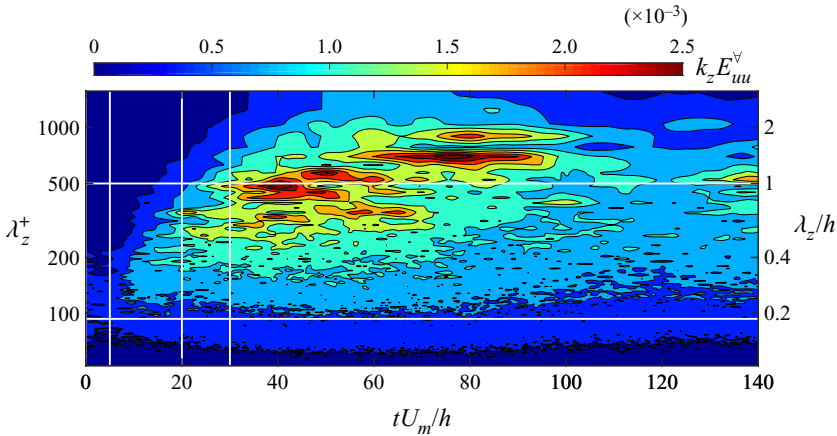
Figure 14. Time evolution of $k_z E_{uu}^{\forall}(t, \lambda_z)$ as a function of λ_z in the lower half-channel. The vertical white lines mark the time instants $t = 5, 20$ and 30.

The evolution of the streamwise velocity fluctuations towards larger scales can be quantified by the time-dependent spanwise energy spectrum, defined as

$$E_{uu}(t, y, k_z) = \frac{1}{L_x} \int_0^{L_x} \left(|\hat{u}(t, x, y, k_z)|^2 + |\hat{u}(t, x, y, -k_z)|^2 \right) \mathrm{d}x. \tag{4.1}$$

The evolution of its integral over the lower half-channel, $E_{uu}^{\forall}(t, \lambda_z)$, is shown in figure 14 as a function of λ_z and of time. The energy is initially concentrated around $100 < \lambda_z^+ < 230$, where the initial perturbations have been introduced, and spreads to wider wavelengths as LSMs are gradually generated. The final peak at $\lambda_z \sim h$ develops for $t \gtrsim 30$, in accordance with figure 13. The numerical experiment evolves to a fully developed turbulent state after $t = 120$, with much lower fluctuations compared with the peaks before $t = 100$.

After confirming that the flow is able to generate LSMs with the only input of initially imposed near-wall streaks, the question of whether streak accumulation is required for this generation is explored by means of the temporal evolution of the correlation (3.14) between the near-wall streak density, $\rho_s(y_1^+ = 13)$, and the wall-normal velocity $\tilde{v}(y_2)$. Figure 15(a) presents the time history of this correlation coefficient $R(t, y_2)$, with an averaging window $\Delta z^+ \approx 200$.

The wall-normal locations for which $R > 0.1$ are confined below $y_2^+ = 100$, implying only local interactions within the buffer layer, and no change can be observed before or after the LSMs appear at $t \approx 30$. Therefore, the conclusion reached in § 3.2 approximately the lack of correlation between the streak density and the outer velocity also applies to the LSM generation process.

The same lack of correlation holds when a delay is introduced in R. The correlation between $\tilde{v}(y_2, t_0)$ and $\rho_s(y_1, t_0 - \Delta t)$ is shown in figure 15(b) as a function of Δt. If the outer LSMs were a result of streak accumulation, as assumed by the bottom-up hypothesis, this correlation should peak at some finite delay, but it is clear from the figure that the correlation maximum is at $\Delta t = 0$, and that it never reaches above $y_2^+ \approx 30$. This again argues against the hypothesis that the formation of outer scales is due to the previous accumulation of streaks in the near-wall region.
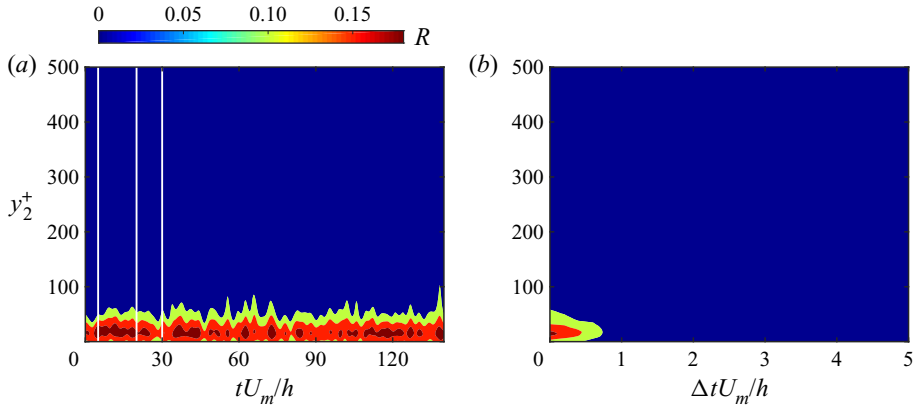
940 A23-18

Figure 15. (*a*) Time history of the correlation $R(\rho_s, \tilde{v})$ with $\Delta z^+ \approx 200$. Vertical white lines mark the time instants $t = 5, 20$ and 30. (*b*) The correlation R between $\tilde{v}(x, y_2, z, t_0)$ and $\rho_s(x - x_{ad}, y_1, z, t_0 - \Delta t)$ as function of Δt. Here $\Delta z^+ \approx 200$. The statistics are compiled by scanning x and z; $t_0 = 30h/U_m$ and $x_{ad} = (u_{ad}(y_2) - u_{ad}(y_1))\Delta t$ is the streamwise offset due to the different advection velocities.

Although this numerical experiment shows that the generation of LSMs does not depend on the accumulation of the near-wall streaks, it could still be possible that the maintenance of the LSMs depends on the existence of large-scale non-uniformities near the wall. This is tested by a second numerical experiment, in which the LSMs below $y^+ = 50$ are artificially removed after the flow has become fully turbulent in the first experiment.

Fourier filtering is applied at $t = 300$ to the lower side of the channel below $y^+ = 50$, to remove the fluctuations of the three velocity components with $\lambda_z > h/2$. The subsequent evolution of the streamwise turbulent kinetic energy at scales $\lambda_z > h$ is displayed in figure 16(*a*). The influence of the filtering gradually rises to $y^+ \approx 100$, whereas new energy appears in the buffer layer at $t \approx 305$, with a local maximum near $t = 308$, possibly reflecting the top-down influence of the LSMs remaining in the outer region. The adjustment of the buffer layer lasts until $t \approx 315$, after which E_{uu} recovers its equilibrium distribution. The time evolution of $k_z E_{uu}$ at $y^+ = 200$ during this recovery process is displayed in figure 16(*b*). The energy peak at $\lambda_z \approx 1.5h$ evolves smoothly with time, and the influence of the disturbed buffer layer can hardly be seen.

This result suggests that the removal of LSMs below $y^+ = 50$ has little impact on the preservation of LSMs in the outer region. Notably, the adjustment time of the buffer layer in response to the sudden filtering is approximately $\Delta t = 15h/U_m$ ($\Delta t^+ \approx 440$), which is of the same order as the average lifetime of LSMs at the present Reynolds number (Lozano-Durán & Jiménez 2014*b*), and should thus be long enough for the LSMs to decay if their maintenance mechanism had been interrupted. Figure 16(*b*) shows that they do not.

In summary, the twin experiments in this section strongly suggest that the production and preservation of LSMs in the outer region do not rely on the existence of large-scale organisation in the near-wall region, in accordance with the results of Flores & Jiménez (2006) and others mentioned in the introduction. They all suggest that the possible bottom-up influence is not essential for the preservation of the outer structures.

5. Summary and conclusions

The inner–outer co-supporting model of Toh & Itano (2005), which had up to now only been studied in turbulent channels with short simulation boxes, has been examined in
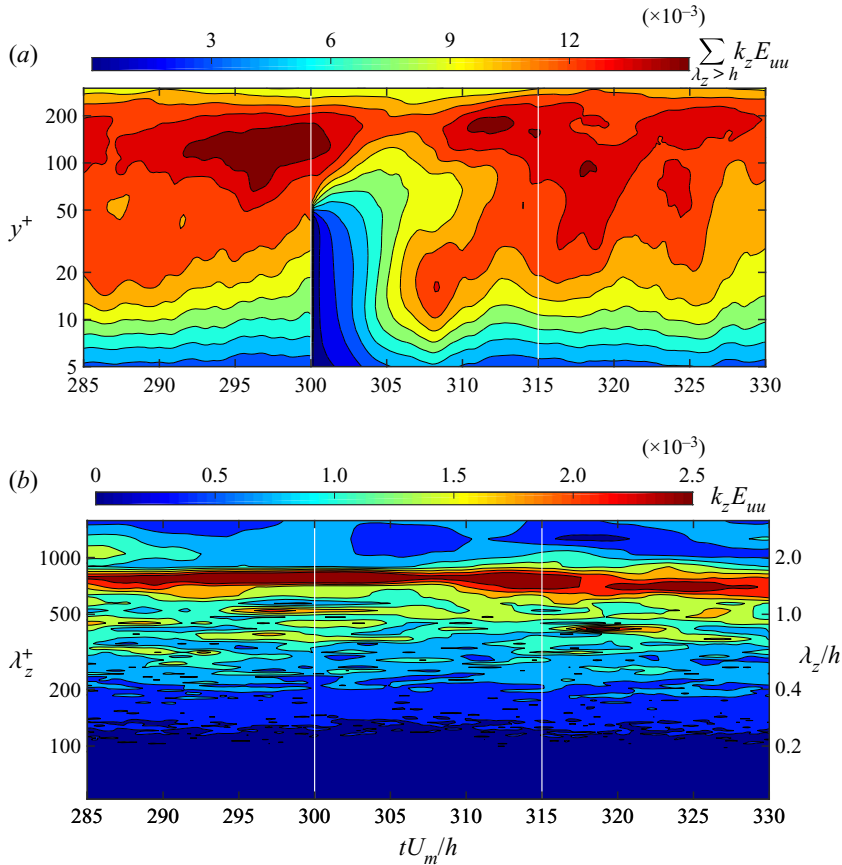
Figure 16. Time evolution of (a) $\sum_{\lambda_z > h} k_z E_{uu}(t, y^+, \lambda_z)$ and (b) $k_z E_{uu}$ at $y^+ = 200$ in the lower half-channel from $t = 285$ to $t = 330$. The vertical white lines are $t = 300$ and $t = 315$.

full-sized simulations at low to moderate Reynolds numbers. The model has three stages: the near-wall streaks drift in the spanwise direction under the influence of the outer LSMs; they accumulate in areas of large-scale velocity convergence; and areas of high streak density lead to the formation of new LSMs.

We have confirmed the first stage by tracking near-wall streaks by a method similar to PIV. The streaks drift spanwise with velocities of the order of $\pm u_\tau$, and this drift is correlated with the large-scale velocity of the outer structures. Moreover, the coupling not only happens between the wall and the largest LSMs. Structures centred at distance y from the wall in the logarithmic layer couple most strongly with the drift of streaks over spanwise distances of $O(y)$, in agreement with the standard model of a hierarchy of wall-attached eddies (Townsend 1961).

The evidence for streak accumulation is less clear, and we have shown that most of the effect observed in Toh & Itano (2005) and Abe *et al.* (2018) is due to their requirement that streaks should have a streamwise velocity lower than the mean profile. When this condition is removed, the streak density becomes fairly uniform, and its correlation with the outer structures mostly disappears. In fact, it even changes sign far enough from the wall. The latter also turns out to be due to the spurious modulating effect of the non-uniform wall shear induced by the large outer scales. When this is taken into account, the correlation

between the outer flow and the streak density is uniformly positive, but mostly restricted to structures below $y^+ \approx 150$, suggesting that the co-supporting cycle is a wall-layer effect that becomes less relevant as the Reynolds number increases. The reason is traced to the lifetime of the streaks, which is too short to couple to higher and wider structures, but which is probably artificially stabilised by the short simulation boxes in Toh & Itano (2005) (interestingly, this possibility was anticipated in that paper, but largely forgotten afterwards).

In addition to the examination and quantification of the top-down influence, the bottom-up branch of the cycle is investigated by means of two numerical experiments that facilitate the artificial isolation of the structures at different scales. The first focuses on the generation process of LSMs, starting from artificially assembled near-wall streaks in an otherwise fluctuation-less flow. The correlation between the streak density and the outer flow changes little before or after the LSM spontaneously appear and their size gradually grows. Moreover, the streak accumulation history hardly influences the appearance of large-scale components of the wall-normal velocity, implying that the streak merging does not have a strong relation with the generation of the LSMs.

A final experiment concentrates on the preservation of existing LSMs. The large-scale component of the velocity fluctuations in the near-wall region is filtered out once the flow is fully established, but the outer LSMs are essentially unaffected during the regeneration of the buffer region. Both experiments argue against the bottom-up branch of the co-supporting hypothesis of Toh & Itano (2005).

Declaration of interests. The authors report no conflict of interest.

Author ORCIDs.
- Zisong Zhou https://orcid.org/0000-0003-3708-1273;
- Chun-Xiao Xu https://orcid.org/0000-0001-5292-8052;
- Javier Jiménez https://orcid.org/0000-0003-0755-843X.

Appendix A. Parameters of the PIV scheme

This appendix tests the effect on the correlation coefficient defined in (3.6) of the interrogation parameters of the PIV drift estimation in § 3.1.

Figure 17(*a*) displays the effect of the measurement interval Δt on the correlation $R(w_s, \partial \tilde{v}/\partial z)$. In general, the correlation drops as Δt grows, and becomes too weak to be useful for $\Delta t^+ \gtrsim 60$. The most probable reason is that the delay acts as a filter that rejects structures with lifetimes shorter than Δt. The lifetime of ejections in the buffer layer is known to be approximately 30 viscous units (Lozano-Durán & Jiménez 2014*b*), independently of the Reynolds number, and this is probably the reason why the correlations in figure 17(*a*) drop rapidly above $\Delta t^+ > 30$. It is also why we choose $\Delta t^+ = 20$ in § 3.1. As in the line contours in figure 5, the dashed red line in figure 17(*a*) is computed using only values at the streak axes. The difference with the solid line, which uses the full field of the drift velocity, is also minor in this case.

Figure 17(*b*) shows the effect of the advection velocity of the interrogation windows, which is relatively small except in extreme cases such as $u_{ad} = 0$. The PIV correlation does not itself use streamwise information, and the estimation of w_s should work as long as the same point of the streak can be identified at the two instants used in the correlation.
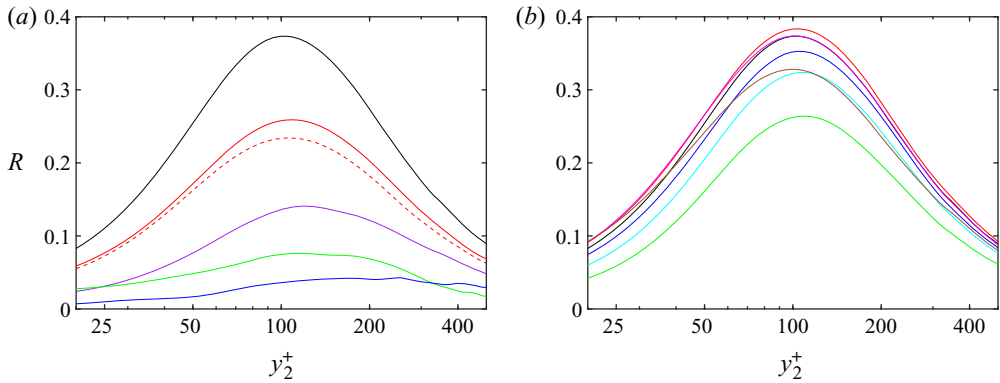
Figure 17. Correlation $R(w_s, \partial\tilde{v}/\partial z)$, as defined in (3.6), against y_2^+. (*a*) At different Δt^+; $u_{ad}^+ = 8.0$; black solid line, $\Delta t^+ = 10.2$; red solid line, 20.3; violet solid line, 40.6; green solid line, 60.8; blue solid line, 101.4. The dashed red line is drawn using only values at the streak axes. (*b*) Correlation against y_2^+ at different streamwise tracking speeds; $\Delta t^+ = 20.3$; green solid line, $u_{ad}^+ = 0$; sky blue solid line, $u_{ad}^+ = 4$; blue solid line, $u_{ad}^+ = 6$; black solid line, $u_{ad}^+ = 8$; red solid line, $u_{ad}^+ = 10$ pink solid line, $u_{ad}^+ = 12$; brown solid line, $u_{ad}^+ = 16$. Both panels are for case M950 and $\Delta z^+ = 214$.

As streaks tend to be long and oriented streamwise, small advection misalignments are not critical, but large advection errors risk mixing the irregularities of the streak geometry, such as meandering, with its spanwise drift. The optimum correlation is obtained in figure 17(*b*) when using the advection velocity obtained elsewhere by physical arguments ($u_{ad}^+ = 8$).

However, it is clear from figure 17 that the largest effect on the correlation is not from the PIV parameters, but from the choice of the correct smoothing filter for the wall distance of interest. As shown by figure 6 in the body of the paper, outer structures of a given height couple most strongly with spanwise regions of a particular width in the buffer layer.

Appendix B. The flow in the upper side of the numerical experiment

This appendix discusses the flow in the upper side of the numerical experiment in §4, where the LSMs appear before the near-wall streaks. Distributions of vortices and streamwise velocity fluctuations before and during the transition are displayed in figure 18. Pairs of large-scale low- and high-speed regions form in the upper half of the channel at $t = 50$, at a time when the small-scale vortical structures are still very rare. The LSMs gradually move closer to the wall after $t = 50$, whereas near-wall structures are still absent and their intensity is progressively enhanced, with energy drawn from the local mean shear. Small-scale vortices are first generated around $t = 60$, in the strongest high-speed regions of the LSMs, accompanied by an increase at the local Re_τ on the upper wall (see figure 11). The generation of vortices then intensifies and quickly spreads to other regions of the upper wall, whose Re_τ grows rapidly. At $t = 68$, the small-scale vortical structures occupy most of the upper wall region, and the near-wall small-scale streaks take their final shape. This evolution suggests that the LSMs can grow and sustain themselves under the influence of the mean velocity profile, even without near-wall streaks.
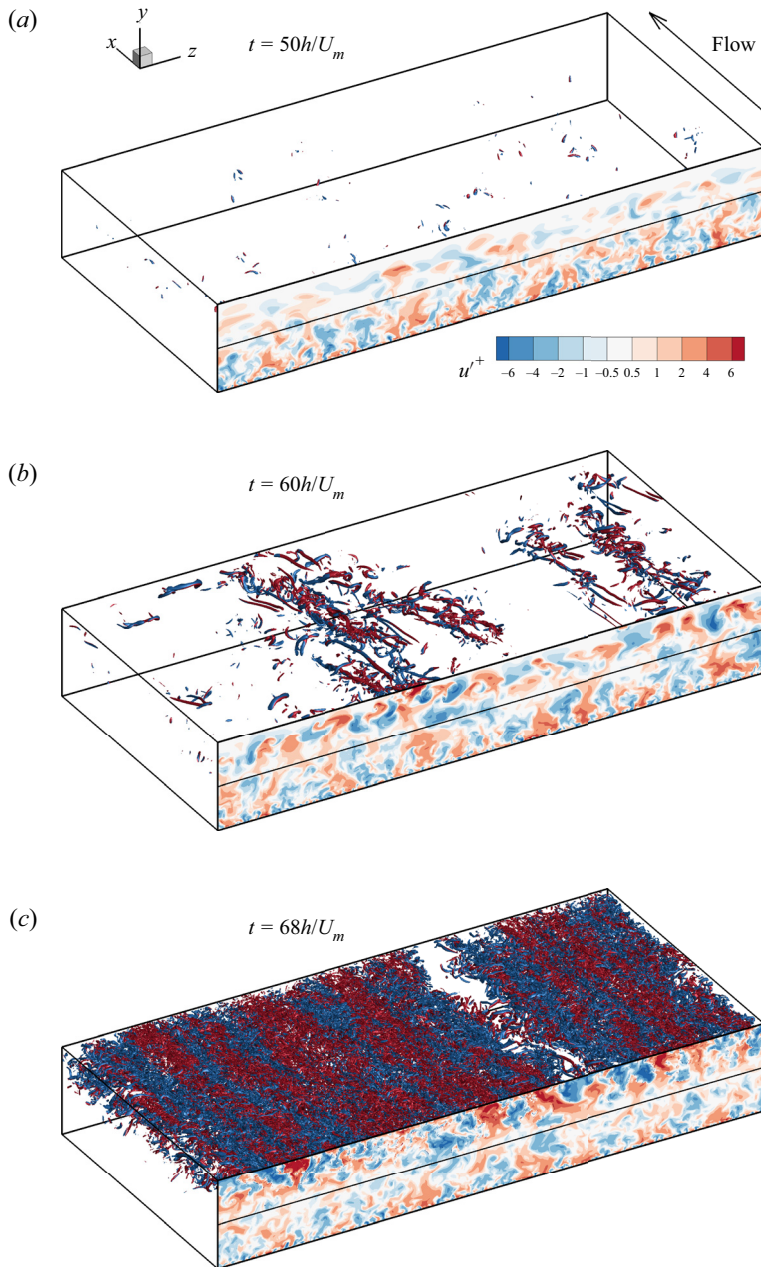
940 A23-22

Figure 18. Time evolution of u' and vortices in the upper half-channel. Length in the x direction is 2π, and in the z direction is 4π. The vortices are displayed by iso-surfaces of the second invariant of the velocity gradient tensor, and coloured red for $u' > 0$ and blue for $u' < 0$. Flow is from bottom right to top left.

REFERENCES

ABE, H., ANTONIA, R. & TOH, S. 2018 Large-scale structures in a turbulent channel flow with a minimal streamwise flow unit. *J. Fluid Mech.* **850**, 733–768.

ABE, H., KAWAMURA, H. & CHOI, H. 2004 Very large-scale structures and their effects on the wall shear-stress fluctuations in a turbulent channel flow up to $Re\tau = 640$. *Trans. ASME J. Fluids Engng* **126** (5), 835–843.

ADRIAN, R.J. 2007 Hairpin vortex organization in wall turbulence. *Phys. Fluids* **19** (4), 041301.

DEL ÁLAMO, J.C. & JIMÉNEZ, J. 2003 Spectra of the very large anisotropic scales in turbulent channels. *Phys. Fluids* **15** (6), L41–L44.

DEL ÁLAMO, J.C. & JIMÉNEZ, J. 2006 Linear energy amplification in turbulent channels. *J. Fluid Mech.* **559**, 205–213.

DEL ÁLAMO, J.C. & JIMÉNEZ, J. 2009 Estimation of turbulent convection velocities and corrections to Taylor's approximation. *J. Fluid Mech.* **640**, 5–26.

DEL ÁLAMO, J.C., JIMÉNEZ, J., ZANDONADE, P. & MOSER, R.D. 2004 Scaling of the energy spectra of turbulent channels. *J. Fluid Mech.* **500**, 135–144.

BALAKUMAR, B.J. & ADRIAN, R.J. 2007 Large- and very-large-scale motions in channel and boundary-layer flows. *Phil. Trans. R. Soc.* A **365** (1852), 665–681.

BALTZER, J.R., ADRIAN, R.J. & WU, X.H. 2013 Structural organization of large and very large scales in turbulent pipe flow simulation. *J. Fluid Mech.* **720**, 236–279.

BUTLER, K.M. & FARRELL, B.F. 1993 Optimal perturbations and streak spacing in wall-bounded shear flow. *Phys. Fluids* A **5**, 774–777.

COSSU, C. & HWANG, Y. 2017 Self-sustaining processes at all scales in wall-bounded turbulent shear flows. *Phil. Trans. R. Soc.* A **375** (2089), 20160088.

DENG, B.-Q. & XU, C.-X. 2012 Influence of active control on STG-based generation of streamwise vortices in near-wall turbulence. *J. Fluid Mech.* **710**, 234–259.

DONG, S., LOZANO-DURÁN, A., SEKIMOTO, A. & JIMÉNEZ, J. 2017 Coherent structures in statistically stationary homogeneous shear turbulence. *J. Fluid Mech.* **816**, 167–208.

DOOHAN, P., WILLIS, A.P. & HWANG, Y. 2021 Minimal multi-scale dynamics of near-wall turbulence. *J. Fluid Mech.* **913**, A8.

FLORES, O. & JIMÉNEZ, J. 2006 Effect of wall-boundary disturbances on turbulent channel flows. *J. Fluid Mech.* **566**, 357–376.

FLORES, O. & JIMÉNEZ, J. 2010 Hierarchy of minimal flow units in the logarithmic layer. *Phys. Fluids* **22** (7), 071704.

GUALA, M., HOMMEMA, S.E. & ADRIAN, R.J. 2006 Large-scale and very-large-scale motions in turbulent pipe flow. *J. Fluid Mech.* **554**, 521–542.

HAMILTON, J., KIM, J. & WALEFFE, F. 1995 Regeneration mechanisms of near-wall turbulence structures. *J. Fluid Mech.* **287**, 317–348.

HOYAS, S. & JIMÉNEZ, J. 2006 Scaling of the velocity fluctuations in turbulent channels up to $Re_\tau = 2003$. *Phys. Fluids* **18**, 011702.

HUTCHINS, N. & MARUSIC, I. 2007a Evidence of very long meandering features in the logarithmic region of turbulent boundary layers. *J. Fluid Mech.* **579**, 1–28.

HUTCHINS, N. & MARUSIC, I. 2007b Large-scale influences in near-wall turbulence. *Phil. Trans. R. Soc.* A **365** (1852), 647–664.

HWANG, Y. & COSSU, C. 2010 Self-sustained process at large scales in turbulent channel flow. *Phys. Rev. Lett.* **105** (4), 044505.

JIMÉNEZ, J. 1998 The largest scales of turbulence. In *CTR Ann. Res. Briefs* (ed. P. Moin, W.C. Reynolds & N.N. Mansour), pp. 137–154. Stanford University.

JIMÉNEZ, J. 2012 Cascades in wall-bounded turbulence. *Annu. Rev. Fluid Mech.* **44**, 27–45.

JIMÉNEZ, J., KAWAHARA, G., SIMENS, M.P., NAGATA, M. & SHIBA, M. 2005 Characterization of near-wall turbulence in terms of equilibrium and 'bursting' solutions. *Phys. Fluids* **17**, 015105.

JIMÉNEZ, J. & MOIN, P. 1991 The minimal flow unit in near-wall turbulence. *J. Fluid Mech.* **225**, 213–240.

JIMÉNEZ, J. & PINELLI, A. 1999 The autonomous cycle of near-wall turbulence. *J. Fluid Mech.* **389**, 335–359.

KIM, J. & HUSSAIN, F. 1993 Propagation velocity of perturbations in channel flow. *Phys. Fluids* A **5**, 695–706.

KIM, K.C. & ADRIAN, R.J. 1999 Very large-scale motion in the outer layer. *Phys. Fluids* **11** (2), 417–422.

KLINE, S.J., REYNOLDS, W.C., SCHRAUB, F.A. & RUNSTADLER, P.W. 1967 The structure of turbulent boundary layers. *J. Fluid Mech.* **30** (4), 741–773.

KWON, Y. & JIMÉNEZ, J. 2021 An isolated logarithmic layer. *J. Fluid Mech.* **916**, A35.

LEE, J.H. & SUNG, H.J. 2011 Very-large-scale motions in a turbulent boundary layer. *J. Fluid Mech.* **673**, 80–120.

LOZANO-DURÁN, A. & JIMÉNEZ, J. 2014a Effect of the computational domain on direct simulations of turbulent channels up to $Re_\tau = 4200$. *Phys. Fluids* **26** (1), 011702.

LOZANO-DURÁN, A. & JIMÉNEZ, J. 2014*b* Time-resolved evolution of coherent structures in turbulent channels: characterization of eddies and cascades. *J. Fluid Mech.* **759**, 432–471.

MARUSIC, I., MATHIS, R. & HUTCHINS, N. 2010*a* High Reynolds number effects in wall turbulence. *Intl J. Heat Fluid Flow* **31** (3), 418–428.

MARUSIC, I., MATHIS, R. & HUTCHINS, N. 2010*b* Predictive model for wall-bounded turbulent flow. *Science* **329** (5988), 193–196.

MATHIS, R., HUTCHINS, N. & MARUSIC, I. 2009 Large-scale amplitude modulation of the small-scale structures in turbulent boundary layers. *J. Fluid Mech.* **628**, 311–337.

MATHIS, R., HUTCHINS, N. & MARUSIC, I. 2011 A predictive inner–outer model for streamwise turbulence statistics in wall-bounded flows. *J. Fluid Mech.* **681**, 537–566.

MCKEON, B. & SHARMA, A. 2010 A critical-layer framework for turbulent pipe flow. *J. Fluid Mech.* **658**, 336–382.

MIZUNO, Y. & JIMÉNEZ, J. 2013 Wall turbulence without walls. *J. Fluid Mech.* **723**, 429–455.

MONTY, J.P., HUTCHINS, N., NG, H.C.H., MARUSIC, I. & CHONG, M.S. 2009 A comparison of turbulent pipe, channel and boundary layer flows. *J. Fluid Mech.* **632**, 431–442.

PUJALS, G., GARCÍA-VILLALBA, M., COSSU, C. & DEPARDON, S. 2009 A note on optimal transient growth in turbulent channel flows. *Phys. Fluids* **21** (1), 015109.

SCHOPPA, W. & HUSSAIN, F. 2002 Coherent structure generation in near-wall turbulence. *J. Fluid Mech.* **453**, 57–108.

SCOVAZZI, G., JIMÉNEZ, J. & MOIN, P. 2001 LES of the very large scales in a $Re_\tau = 920$ channel. In *Proc. Div. Fluid Dyn.* (ed. P. Moin), pp. KF–5. American Physical Society.

SMITH, C.R. & METZLER, S.P. 1983 The characteristics of low speed streaks in the near wall region of a turbulent boundary layer. *J. Fluid Mech.* **129**, 27–54.

TANAHASHI, M., KANG, S.-J., MIYAMOTO, T., SHIOKAWA, S. & MIYAUCHI, T. 2004 Scaling law of fine scale eddies in turbulent channel flow at to $Re_\tau = 800$. *Intl J. Heat Fluid Flow* **25**, 331–340.

TOH, S. & ITANO, T. 2005 Interaction between a large-scale structure and near-wall structures in channel flow. *J. Fluid Mech.* **524**, 249–262.

TOWNSEND, A.A. 1961 Equilibrium layers and wall turbulence. *J. Fluid Mech.* **11** (1), 97–120.

TOWNSEND, A.A. 1976 *The Structure of Turbulent Shear Flow*, 2nd edn. Cambridge University Press.

TUERKE, F. & JIMÉNEZ, J. 2013 Simulations of turbulent channels with prescribed velocity profiles. *J. Fluid Mech.* **723**, 587–603.

ZHANG, C. & CHERNYSHENKO, S.I. 2016 Quasisteady quasihomogeneous description of the scale interactions in near-wall turbulence. *Phys. Rev. Fluids* **1**, 014401.